Global stability analysis of axisymmetric boundary layer over a circular cone

Ramesh Bhoraniya* and Narayanan Vinod†

Department of Mechanical Engineering, Indian Institute of Technology Gandhinagar, Palaj, Gandhinagar, Gujarat 382355, India

(Received 26 August 2016; published 15 June 2017)

This paper presents a linear global stability analysis of the incompressible axisymmetric boundary layer on a circular cone. The base flow is considered parallel to the axis of the cone at the inlet. The angle of attack is zero and hence the base flow is axisymmetric. A favorable pressure gradient develops in the streamwise direction due to cone angle. The Reynolds number is calculated based on the cone radius a at the inlet and freestream velocity U_∞. The base flow velocity profile is fully nonparallel and nonsimilar. Linearized Navier-Stokes equations (LNSEs) are derived for the disturbance flow quantities in the spherical coordinates. The LNSEs are discretized using the Chebyshev spectral collocation method. The discretized LNSEs along with the homogeneous boundary conditions form a general eigenvalues problem. Arnoldi's iterative algorithm is used for the numerical solution of the general eigenvalues problem. The global temporal modes are computed for the range of Reynolds number from 174 to 1046, semicone angles 2°, 4°, and 6°, and azimuthal wave numbers from 0 to 5. It is found that the global modes are more stable at higher semicone angle α, due to the development of favorable pressure gradient. The effect of transverse curvature is reduced at higher α. The spatial structure of the eigenmodes shows that the flow is convectively unstable. The spatial growth rate A_x increases with an increase in α from 2° to 6°. Thus, the effect of an increase in α is to reduce the temporal growth rate ω_i and increase the A_x of the global modes at a given Reynolds number.

DOI: 10.1103/PhysRevFluids.2.063901

I. INTRODUCTION

The laminar-turbulent transition in boundary layers has been a subject of interest to many researchers in the past few decades. It is important to understand the onset of transition in boundary layers as the flow pattern and its effects are very different in laminar and turbulent flows. For example, the drag force in turbulent flows is much higher than that of laminar flows. At low freestream levels the boundary layers undergo transition through the classical Tollmien-Schlichting (TS) wave mechanism. The amplification of the disturbance waves is the primary step in the transition process and this is studied in the linear stability analysis. The results of the stability analysis and the prediction of transition onset are very useful in hydrodynamics and aerodynamics applications such as submarines, torpedoes, rockets, and missiles.

The linear stability analysis of shear flows with a parallel flow assumption is understood using the solution of the Orr-Sommerfeld equation [1]. It is known that the stability characteristics in a boundary layer are strongly influenced by various factors such as pressure gradient, surface curvature, and freestream turbulence level.

The boundary layer formed over a right circular cone is axisymmetric and it is qualitatively different from a flat-plate boundary layer. The boundary layer on a circular cone develops continuously in the spatial directions, hence the parallel flow assumption is not valid. Due to the wall-normal velocity component, the boundary layer is nonparallel. The instability analysis of such two-dimensional base flow is called global stability analysis [2]. The literature on the instability

*Also at Department of Mechanical Engineering, Faculty of Engineering, Marwadi Education Foundations Group of Institutions, Rajkot, India.

†vinod@iitgn.ac.in

analysis of the incompressible axisymmetric boundary layer is sparse. The reported literature on the instability of the axisymmetric boundary layer is limited to local stability analysis only.

Rao performed local stability analysis on the axisymmetric boundary layer and found that axisymmetric disturbances are more stable than three-dimensional disturbances [3]. Tutty and Price [4] found that the critical Reynolds number of helical modes (nonaxisymmetric) increases with the azimuthal wave number N. The critical Reynolds number is 12 439 and 1060 for $N = 1$ and $N = 0$ modes, respectively. The helical modes $N = 1$, 2, and 3 are more unstable than the axisymmetric mode $N = 0$. Vinod performed stability analysis with a parallel flow assumption and found that the azimuthal mode $N = 2$ is linearly stable for a small value of curvature only [5]. The mode with azimuthal wave number $N = 1$ is unstable over a large length of the cylinder and is always found stable for curvature greater than unity. The transverse curvature has a significant damping effect on the disturbances. The effect of transverse curvature and streamline curvature was studied by Malik and Poll on an incompressible boundary layer and concluded that it has a strong stabilizing effect on the perturbations [6]. The secondary stability analysis was performed by Vinod and Govindarajan on an incompressible axisymmetric boundary layer and found that in the laminar regime the flow is always stable to secondary disturbances at higher curvature [7].

The stability analysis of an axisymmetric boundary layer with a rotating cylinder is also reported in the literature. Petrov studied the stability of the boundary layer with a rotating cylinder [8]. Kao and Chao [9] found that the transverse curvature has a stabilizing effect in rotational flow. Herrada *et al.* [10] showed that nonparallel effects are important in the stability of a rotating thin cylinder. Muralidhar *et al.* obtained stability results for the rotating cylinder with a high Reynolds number and found that the wall jet effect becomes stronger with an increase in rotation rate [11].

The global stability analysis for hypersonic and supersonic flows over a circular cone is reported in the literature. The linear stability analysis was performed by L.M. Mack for supersonic flow past a sharp circular cone for a range of Mach numbers [12]. Malik studied the local and global stability characteristics of hypersonic boundary layers on a circular cone. He found the existence of stable modes in the limit of vanishing Mach number [13]. Malik and Spall presented equations of base flow for a viscous compressible axisymmetric boundary layer. They performed stability analysis for axisymmetric and three-dimensional (3D) disturbances. In the experimental study of TS and Gortler instabilities, they found that transverse curvature has a damping effect on axisymmetric disturbances and a destabilizing effect on 3D helical modes [14]. Duck reported that the transverse effect becomes very small when the radius is much larger than the boundary layer thickness [15]. Duck and Hall reported for the supersonic axisymmetric boundary layer that the neutral stability boundaries show no similarity for the strong effect of transverse curvature [16]. Duck studied supersonic flow past a circular cylinder and found that with the increase in curvature the first inviscid unstable mode disappears rapidly and the growth rate of the second mode is reduced [17]. Duck and Shaw continued this study on 3D disturbances for the supersonic laminar boundary layer on a cone and computed the inviscid growth rate. They also identified the least unstable disturbance as a different mode of instability on a sharp cone [18]. In the supersonic and hypersonic boundary layers there exist higher acoustic instability modes with higher frequencies in addition to the first instability mode [19]. It has been confirmed by experiments that the two-dimensional Mack mode dominates in the hypersonic boundary layer [20–22]. Experimental results show that leading bluntness affects the transition location significantly in a circular cone [23].

In the case of an axisymmetric boundary layer on a circular cylinder, the transverse curvature effect increases in the streamwise direction, which helps in stabilizing the flow. In the case of an axisymmetric boundary layer on a circular cone, the body radius of the cone increases at a higher rate than that of the boundary layer thickness δ and hence the transverse curvature effect δ/a is reduced in the streamwise direction, as shown in Fig. 1. However, a favorable pressure gradient develops in the streamwise direction due to the cone angle α. Thus, it becomes interesting to study the combined effect of transverse curvature and pressure gradient on the stability characteristics. The two-dimensional global modes have also been computed for the flat-plate boundary layer by some investigators [24–26]; however, here we carry out global stability analysis of the incompressible

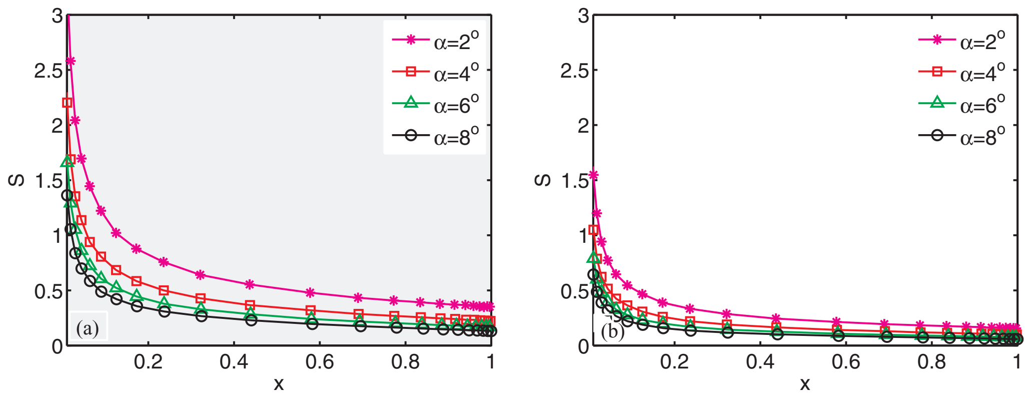

FIG. 1. Variation of the transverse curvature ($S = \delta/a$) in the streamwise direction for different semicone angles α for (a) Re = 174 and (b) Re = 872.

boundary layer over a circular cone. In the present work we analyze the stability of the most unstable temporal mode, i.e., we perform a modal analysis, which is the preferred route in a low freestream turbulence level. The main aim of this paper is to study the global stability characteristics of the axisymmetric boundary layer on a circular cone and the effect of the transverse curvature and pressure gradient on the stability characteristics.

II. PROBLEM FORMULATION

The governing equations for the perturbed flow quantities are obtained from the Navier-Stokes equations of the base flow and perturbed flow quantities in the spherical coordinates (r,θ,ϕ). The governing equations are normalized by the radius of the cone (a) at the inflow boundary and freestream velocity U_∞. The linearized Navier-Stokes equations (LNSEs) for perturbed flow quantities are obtained by subtraction and subsequent linearization. The base flow is axisymmetric due to a zero angle of attack at the inflow boundary. The Reynolds number is computed based on the radius a and freestream velocity U_∞,

$$R_e = \frac{U_\infty a}{\nu}, \tag{1}$$

where a is the surface radius of the cone at inflow and ν is the kinematic viscosity. The flow quantities are presented as the sum of the base flow and the perturb quantities as

$$\begin{aligned} \overline{U_r} &= U_r + u_r, \quad \overline{U_\theta} = U_\theta + u_\theta, \\ \overline{U_\phi} &= 0 + u_\phi, \quad \overline{P} = P + p. \end{aligned} \tag{2}$$

The disturbances are considered in normal mode form and vary in the radial (r) and polar (θ) directions. Thus the disturbances having periodic nature in the azimuthal (ϕ) direction,

$$\mathbf{q}(r,\theta,t) = \hat{\mathbf{q}}(r,\theta)e^{[i(N\phi-\omega t)]}, \tag{3}$$

where $\mathbf{q} = [u_r,u_\theta,u_\phi,p]$, $\mathbf{Q} = [U_r,U_\theta,U_\phi,P]$, $\overline{\mathbf{Q}} = [\overline{U}_r,\overline{U}_\theta,\overline{U}_\phi,\overline{P}]$, r is the radial coordinate, θ is the polar coordinate, ϕ is the azimuthal coordinate, ω is the circular frequency, N is the azimuthal wave number, with

$$\begin{aligned} &\frac{\partial u_r}{\partial t} + U_r\frac{\partial u_r}{\partial r} + u_r\frac{\partial U_r}{\partial r} + \frac{U_\theta}{r}\frac{\partial u_r}{\partial \theta} + \frac{u_\theta}{r}\frac{\partial U_r}{\partial \theta} - u_\theta\frac{2U_\theta}{r} + \frac{\partial p}{\partial r} \\ &-\frac{1}{\mathrm{Re}}\left[\nabla^2 u_r - \frac{2u_r}{r^2} - \frac{2}{r^2}\frac{\partial u_\theta}{\partial \theta} - \frac{2\cot\theta}{r^2}u_\theta - \frac{2}{r^2\sin\theta}\frac{\partial u_\phi}{\partial \phi}\right] = 0, \end{aligned} \tag{4}$$

$$\frac{\partial u_\theta}{\partial t} + U_r \frac{\partial u_\theta}{\partial r} + u_r \frac{\partial U_\theta}{\partial r} + \frac{U_\theta}{r}\frac{\partial u_\theta}{\partial \theta} + \frac{u_\theta}{r}\frac{\partial U_\theta}{\partial \theta} + u_\theta \frac{U_r}{r} + u_r \frac{U_\theta}{r}$$
$$+\frac{1}{r}\frac{\partial p}{\partial \theta} - \frac{1}{\mathrm{Re}}\left[\nabla^2 u_\theta + \frac{2}{r^2}\frac{\partial u_r}{\partial \theta} - \frac{u_\theta}{r^2 \sin^2\theta} - \frac{2\cot\theta}{r^2\sin\theta}\frac{\partial u_\phi}{\partial \phi}\right] = 0, \tag{5}$$

$$\frac{\partial u_\phi}{\partial t} + U_r \frac{\partial u_\phi}{\partial r} + \frac{U_\theta}{r}\frac{\partial u_\phi}{\partial \theta} + u_\phi \frac{U_r}{r} + u_\phi \frac{U_\theta \cot\theta}{r} + \frac{1}{r\sin\theta}\frac{\partial p}{\partial \phi}$$
$$-\frac{1}{\mathrm{Re}}\left[\nabla^2 u_\phi + \frac{2}{r^2\sin\theta}\frac{\partial u_\phi}{\partial \phi} - \frac{u_\phi}{r^2\sin\theta} + \frac{2\cot\theta}{r^2\sin\theta}\frac{\partial u_\phi}{\partial \phi}\right] = 0, \tag{6}$$

$$\frac{\partial u_r}{\partial r} + \frac{2u_r}{r} + \frac{1}{r}\frac{\partial u_\theta}{\partial \theta} + \frac{u_\theta \cot\theta}{r} + \frac{1}{r\sin\theta}\frac{\partial u_\phi}{\partial \phi} = 0, \tag{7}$$

where

$$\nabla^2 = \frac{\partial}{\partial r^2} + \frac{2}{r}\frac{\partial}{\partial r} + \frac{1}{r^2}\frac{\partial}{\partial \theta^2} + \frac{\cot\theta}{r^2}\frac{\partial}{\partial \theta} + \frac{1}{r^2\sin^2\theta}\frac{\partial}{\partial \phi^2}. \tag{8}$$

A. Boundary conditions

No-slip and no-penetration boundary conditions are considered at the surface of the cone. The magnitude of all the disturbance velocity components are zero at the solid surface of the cone due to the viscous effect,

$$u_r(r,\theta_{\min}) = 0, \quad u_\theta(r,\theta_{\min}) = 0, \quad u_\phi(r,\theta_{\min}) = 0. \tag{9}$$

The disturbance flow quantities are expected to vanish at the freestream far away from the solid surface of the cone. The homogeneous Dirichlet conditions are applied to all velocity and pressure disturbances at the freestream,

$$\begin{aligned} u_r(r,\theta_{\max}) = 0, &\quad u_\theta(r,\theta_{\max}) = 0, \\ u_\phi(r,\theta_{\max}) = 0, &\quad p(r,\theta_{\max}) = 0. \end{aligned} \tag{10}$$

The boundary conditions are not straightforward in the streamwise direction for global stability analysis because it is very difficult to get exact information about the incoming and outgoing disturbance flow quantities. Here we are interested in the disturbances evolving within the basic flow field only. Therefore, we considered the homogeneous Dirichlet boundary conditions for disturbance velocity components at the inflow boundary as suggested by Theofilis [2,27]. However, the boundary conditions based on the incoming and outgoing wave information can be applied at the inflow and outflow boundaries [28]. Such conditions impose a wavelike nature of the disturbances and so they are more restrictive in nature, which is not appropriate from a physical point of view. An even streamwise wave number α is not known initially in the case of the global stability analysis. In such conditions linear extrapolation is appropriate and several investigators have implemented it as it is the least restrictive in nature [2,29]. The two-dimensional eigenvalues problem is solved with linear extrapolation at the outflow boundary,

$$u_r(r_{\mathrm{in}},\theta) = 0, \quad u_\theta(r_{\mathrm{in}},\theta) = 0, \quad u_\phi(r_{\mathrm{in}},\theta) = 0, \tag{11}$$

$$u_{r_{n-2}}[r_n - r_{n-1}] - u_{r_{n-1}}[r_n - r_{n-2}] + u_{r_n}[r_{n-1} - r_{n-2}] = 0. \tag{12}$$

The same extrapolation conditions for u_θ and u_ϕ can be written as per Eqs. (11) and (12). The boundary conditions for pressure do not exist physically at the wall of the cone surface. The compatibility conditions are imposed on the wall of the cone, derived from the governing stability equations only [2,30],

$$\frac{\partial p}{\partial r} = \frac{1}{\mathrm{Re}}\left[\nabla^2 u_r - \frac{2}{r^2}\frac{\partial u_\theta}{\partial \theta}\right] - U_r\frac{\partial u_r}{\partial r} - \frac{U_\theta}{r}\frac{\partial u_r}{\partial \theta}, \tag{13}$$

$$\frac{1}{r}\frac{\partial p}{\partial \theta} = \frac{1}{\mathrm{Re}}\left[\nabla^2 u_\theta + \frac{2}{r^2}\frac{\partial u_r}{\partial \theta}\right] - U_r\frac{\partial u_\theta}{\partial r} - \frac{U_\theta}{r}\frac{\partial u_\theta}{\partial \theta}. \tag{14}$$

We use Chebyshev spectral collocation discretization in the streamwise (r) and wall-normal (θ) directions, which are given by

$$r_{\mathrm{Cheb}} = \cos\left(\frac{\pi i}{n}\right) \quad \text{for } i = 0,1,2,3,\ldots,n, \tag{15}$$

$$\theta_{\mathrm{Cheb}} = \cos\left(\frac{\pi j}{m}\right) \quad \text{for } j = 0,1,2,3,\ldots,m, \tag{16}$$

where n and m are the total number of collocation points in the radial (r) and polar (θ) directions. The grid resolution is improved by a grid stretching algorithm in the wall-normal direction,

$$\theta_{\mathrm{real}} = \frac{\theta_i L_\theta (1 - \theta_{\mathrm{Cheb}})}{L_\theta + \theta_{\mathrm{Cheb}}(L_\theta - 2\theta_i)}. \tag{17}$$

In the transformed space, equal numbers of collocation points lie on either side of a predefined point θ_i.

As the nonuniform grid distribution is not suitable in the streamwise direction [31], we transformed it into a uniform distribution using

$$r_{\mathrm{map}} = \frac{\sin^{-1}(\alpha_m r_{\mathrm{Cheb}})}{\sin^{-1}(\alpha_m)}. \tag{18}$$

This minimizes Gibbs oscillations also. Thus, the discretized governing stability equations (LNSEs) can be expressed as a general eigenvalue problem. The operator of the governing equations forms matrices A and B as shown by Eq. (20), where A and B are real matrices of size $nm \times nm$,

$$\begin{bmatrix} A_{11} & A_{12} & A_{13} & A_{14} \\ A_{21} & A_{22} & A_{23} & A_{24} \\ A_{31} & A_{32} & A_{33} & A_{34} \\ A_{41} & A_{42} & A_{43} & A_{44} \end{bmatrix} \begin{bmatrix} u_r \\ u_\theta \\ u_\phi \\ p \end{bmatrix} = i\omega \begin{bmatrix} B_{11} & B_{12} & B_{13} & B_{14} \\ B_{21} & B_{22} & B_{23} & B_{24} \\ B_{31} & B_{32} & B_{33} & B_{34} \\ B_{41} & B_{42} & B_{43} & B_{44} \end{bmatrix} \begin{bmatrix} u_r \\ u_\theta \\ u_\phi \\ p \end{bmatrix}, \tag{19}$$

$$[A][\phi] = i\omega[B][\phi], \tag{20}$$

where ϕ is the eigenvector of the disturbance amplitudes u_r, u_θ, and u_ϕ, and p and $i\omega$ are the eigenvalues.

B. Solution of general eigenvalues problem

The general solution of Eq. (20) gives nm eigenvalues. In a shear flow, only very few modes are important and moreover in a modal analysis the stability is dictated by the most unstable eigenmode only. Hence we look only for the few modes that are close to the least stable eigenmode. We employ Arnoldi's algorithm, which uses the Krylov subspace method, to compute the important eigenvalues only,

$$(A - \lambda B)^{-1} B\phi = \mu\phi \quad \text{for } \mu = \frac{1}{i\omega - \lambda}, \tag{21}$$

where λ is the shift parameter and μ is the eigenvalues of the converted problem. The Krylov subspace is computed by successive resolution of a linear system with a matrix $(A - \lambda B)$, using lower-upper decomposition. The computed spectrum is always near the shift parameter. The good

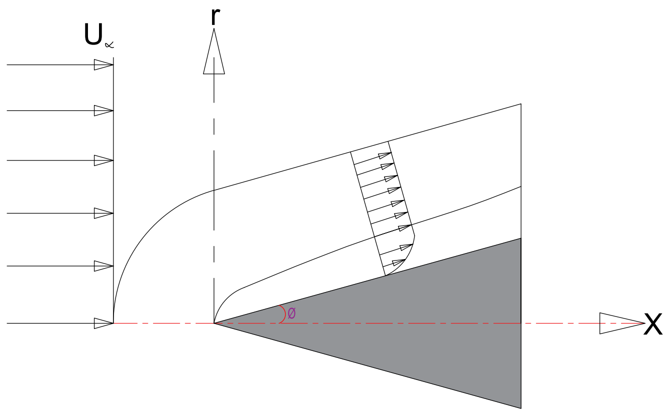

FIG. 2. Schematic diagram of the axisymmetric boundary layer on a circular cone.

approximation of the shift parameter reduces the number of iterations to converge the solution to the required accuracy level. However, a larger size of subspace makes the solution almost independent of the shift parameter λ. We tested the code for several values of shift parameter. However, we have taken the maximum number of iterations equal to 300, hence convergence of the solution may not be affected by the shift parameter. Given the large subspace size of $k = 250$, part of the spectrum for our instability analysis could be recovered in the one computation that took about 4 h on Intel Xeon CPU E5 26500, 2.00 GHz×18.

III. BASE FLOW SOLUTION

Steady incompressible Navier-Stokes equations are numerically solved for an axisymmetric domain using the finite-volume code ANSYS FLUENT to get a base flow velocity profile. The axial and radial dimensions of the axisymmetric model are taken as 1 and 0.5 m, respectively, as shown Fig. 2. The incoming flow streamlines are parallel to the axis of the cone,

$$U\frac{\partial U}{\partial x} + V\frac{\partial U}{\partial r} = -\frac{\partial P}{\partial x} + \frac{1}{R_e}\left(\frac{\partial^2 U}{\partial x^2} + \frac{1}{r}\frac{\partial U}{\partial r} + \frac{\partial^2 U}{\partial r^2}\right), \tag{22}$$

$$U\frac{\partial V}{\partial x} + V\frac{\partial V}{\partial r} = -\frac{\partial P}{\partial r} + \frac{1}{R_e}\left(\frac{\partial^2 V}{\partial x^2} + \frac{1}{r}\frac{\partial V}{\partial r} + \frac{\partial^2 V}{\partial r^2}\right), \tag{23}$$

$$\frac{\partial U}{\partial x} + \frac{\partial V}{\partial r} + \frac{V}{r} = 0. \tag{24}$$

The following boundary conditions are applied in the streamwise direction at the inflow and outflow boundary:

$$U(0,r) = 0, \quad V(0,r) = 0, \tag{25}$$

$$\frac{\partial U}{\partial x} = 0, \quad \frac{\partial V}{\partial x} = 0, \quad P = 0. \tag{26}$$

The steady Navier-Stokes equations are solved using the SIMPLE algorithm with underrelaxation to get the stable solution. The spatial discretization of the Navier-Stokes equations are done using a QUICK scheme, which is a weighted average of the second-order upwind scheme and the second-order central scheme. The thus obtained base velocity profile is interpolated to a spectral grid using cubic spline interpolation. The simulation was started initially with a coarse grid size of 250 and 125 grid points in the axial and radial directions, respectively. The grid was refined with a factor of

TABLE I. Grid convergence study for the base flow obtained using U ($x = 0.5$ and $r = 0.038\,965$) and V ($x = 0.5$ and $r = 0.038\,965$) for $U_\infty = 0.1$ m/s. The grid refinement ratio α in each direction is 1.4142. The relative error ϵ and grid convergence index $\mathcal{G}$ are calculated using two consecutive grid sizes. The j and $j+1$ represent course and fine grids, respectively. Here $\epsilon = \frac{f_j - f_{j+1}}{f_j} \times 100$ and $\mathcal{G}(\%) = 3[\frac{f_j - f_{j+1}}{f_{j+1}(\alpha^n - 1)}] \times 100$, where $n = \log_{10}[\frac{f_j - f_{J+1}}{f_{j+1} - f_{j+2}}]/\log_{10}(\alpha)$. Mesh 1 is a 707×355 grid, mesh 2 is a 500×250 grid, mesh 3 is a 355×177 grid, and mesh 4 is a 250×125 grid.

Mesh	U	ϵ (%)	$\mathcal{G}$ (%)	V	ϵ (%)	$\mathcal{G}$ (%)
1	0.087225	0.008	0.038	0.005893	0.017	0.051
2	0.087213	0.0287	0.080	0.005892	0.034	0.1028
3	0.087188	0.0510	0.144	0.005890	0.068	0.2037
4	0.087143			0.005886		

1.4142 in each direction. The discretization error was calculated through a grid convergence index (GCI) study on four consecutive refined grids [32]. The monotonic convergence is obtained for all the grids as expected. The error and GCI are computed for two different field values U ($x = 0.5$ and $r = 0.038965$) and V ($x = 0.5$ and $r = 0.038965$) near the solid boundary where the gradient is higher. The GCI and error were computed for four different grids as shown in Table I. The error between mesh 1 and mesh 2 is too small. The GCI has also decreased with the refinement of the grids. Thus, the solution has converged monotonically towards the grid-independent one. The further refinement in the grids will hardly improve the accuracy of the solution while it increases the time for the computations. The distribution of the grid is geometric in both directions. The computed convergence orders for U and V are 1.98 and 2.01, in good agreement with the second-order discretization scheme used in the finite-volume code ANSYS FLUENT. A sufficiently large domain height is selected in the radial direction, i.e., 0.5 m. Thus, mesh 1 is used to compute the base flow velocity profile in all the stability results presented here. Figures 3 and 4 show the contour plot and velocity profile on the transformed coordinates ξ and η. The velocity profile is qualitatively similar to that of Garrett and Peake [33]. The base velocity field is transformed to spherical coordinates to perform global stability computations.

IV. CODE VALIDATION

To validate the global stability results for the incompressible flow over a circular cone, a blunt cone with a very small semicone angle $\alpha = 10^{-12}$ is considered. Thus the geometry of the circular cylinder and a blunt cone is similar due to the very small semicone angle α as shown in Fig. 5. A rectangle *epqr* shows the computational domain for the cylindrical coordinates and *efgh* shows that for spherical coordinates. Here L_x and L_r are the streamwise domain length for cylindrical and spherical coordinates. The stability equations for the axisymmetric flow over the circular cylinder and circular cone are derived in polar cylindrical coordinates and spherical coordinates, respectively. The Reynolds number is computed based on the body radius a at the inflow and freestream velocity for both cases. The streamwise and wall-normal extent of the domain is also the same for both domains. Dirichlet boundary conditions are applied on the disturbance amplitudes in the wall-normal direction at the wall surface and the freestream. The global stability results for the axisymmetric boundary layer on a circular cylinder with Robin and periodic boundary conditions have already been validated against the local stability results for the axisymmetric ($N = 0$) and the helical ($N = 1$) modes [34]. So we compare the global stability results of the cone and cylinder with the Robin and periodic boundary conditions. Robin and periodic boundary conditions are considered for the blunt cone with a very small semicone angle α and the same Reynolds number, streamwise wave number, and streamwise location as of circular cylinder. Figure 6 shows a comparison of the eigenspectrum and

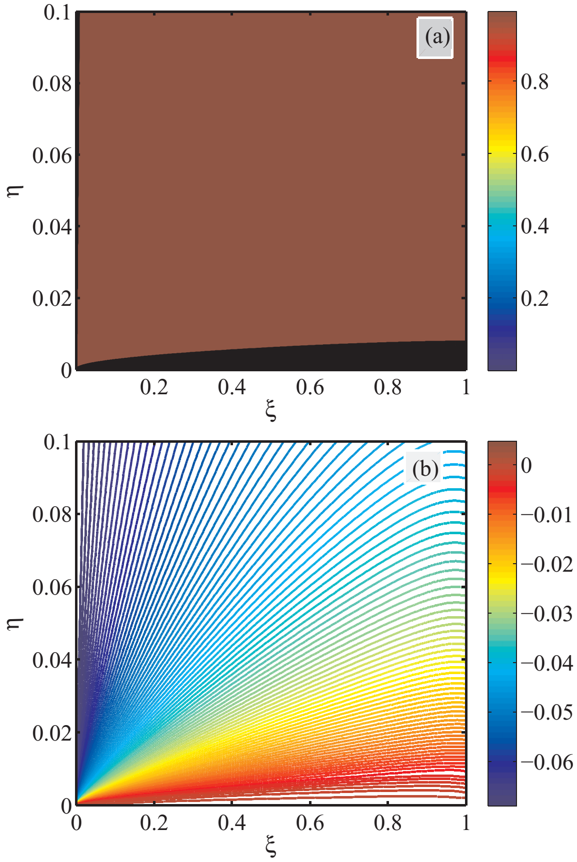

FIG. 3. Base flow contour plot for (a) streamwise U_ξ and (b) wall-normal U_η velocity components for semicone angle $\alpha = 4^\circ$ and Re = 698. The Reynolds number is calculated based on the body radius of the cone a at inlet of the domain. The velocity profile is interpolated to spectral grids for stability analysis. The actual domain height is taken as 0.5 m in the wall-normal direction for base flow computations. Here ξ and η are the coordinates in the streamwise and wall-normal directions, respectively.

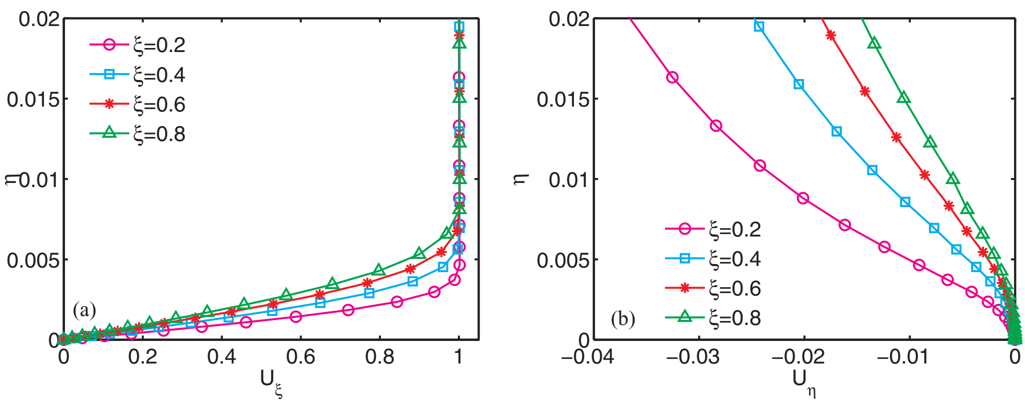

FIG. 4. Base flow velocity profile at different streamwise locations for (a) streamwise velocity U_ξ and (b) wall-normal velocity U_η for the same parameters as in Fig. 3.

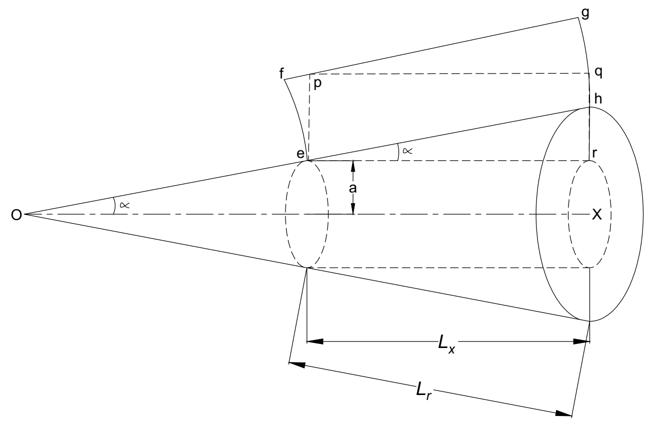

FIG. 5. Computational domain for global stability analysis of the axisymmetric boundary layer over a circular cone and cylinder for very small semicone angle α. The domain is modeled in cylindrical (dashed line) and spherical (solid line) coordinates for flow over the cylinder and cone, respectively.

Fig. 7 shows a comparison of the real parts of the eigenfunctions for the least stable eigenmode. The resulting eigenspectrum and eigenfunctions are in good agreement for the axisymmetric boundary layer formed on the circular cylinder and cone.

We also compare the global stability results of the circular cone and cylinder with the Dirichlet boundary conditions at the inflow boundary and extrapolation conditions at the outflow boundary. Figure 8 shows a comparison of the eigenspectrum of the global stability analysis of the axisymmetric boundary layer over a circular cone and cylinder for $N = 0$ and $\mathrm{Re} = 1000$. The discrete and continuous parts of the spectrum are in excellent agreement with each other. Figure 9 shows a comparison of the eigenfunctions for the least stable eigenmode at the same streamwise location. The eigenfunctions are also in good agreement with each other.

V. RESULTS AND DISCUSSION

The stability computations are performed for semicone angles $\alpha = 2^\circ, 4^\circ$, and 6°, $\mathrm{Re} = 174$–1047, and azimuthal wave number $N = 0$–5. The domain size in the polar (wall-normal) direction is taken

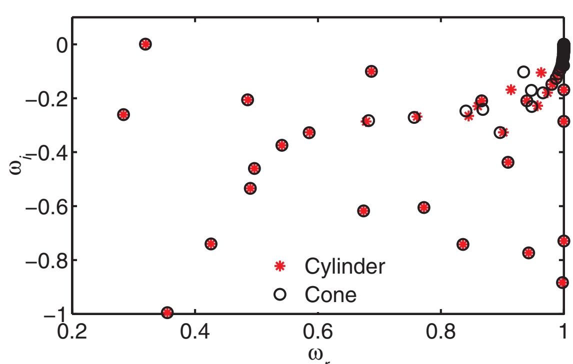

FIG. 6. Comparison of the eigenspectrum for the global stability analysis of the axisymmetric boundary layer over a circular cone and cylinder for the axisymmetric mode ($N = 0$) with Robin and periodic boundary conditions at the inlet and outlet. The Reynolds number based on the body radius at the inflow is $\mathrm{Re} = 12\,439$.

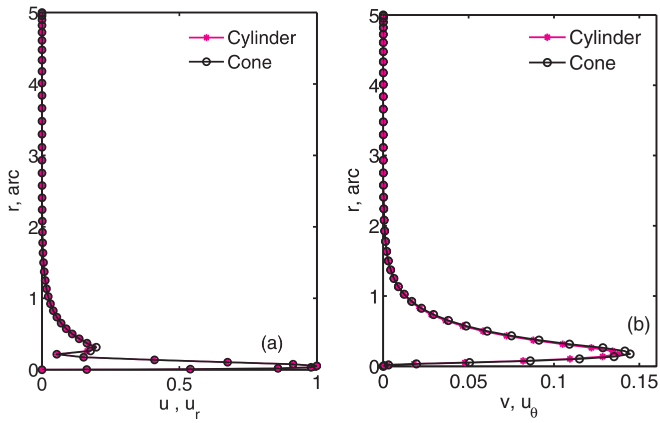

FIG. 7. Comparison of the real parts of the eigenfunction's (a) streamwise u and u_r and (b) wall-normal v and u_θ for the axisymmetric boundary layer on a circular cone and cylinder with Robin and periodic conditions.

as $L_\theta = 12^\circ$. The streamwise (radial) length is taken 0.75 m. The number of collocation points taken in the radial and polar directions are $n = 121$ and $m = 121$, respectively. The general eigenvalues problem is solved using Arnoldi's iterative algorithm. The computed eigenvalues are accurate up to three decimal points. Additional lower-resolution cases are also run to verify the monotonic convergence of the solution. Arnoldi's iterative algorithm is used to solve the general eigenvalues problem. Heavy sponging is applied at the outflow boundary to prevent spurious reflection. The selected global eigenmodes are also checked for the spurious mode.

A. Grid convergence study

A grid convergence study was performed to check the accuracy level of the solution and appropriate grid size. Table II shows the values of two leading eigenvalues computed for Re $= 349$, $N = 1$, and semicone angle $\alpha = 2^\circ$ using three different grid sizes. The grid resolution was successively improved by a factor of 1.14 in the radial and polar directions. The real and imaginary

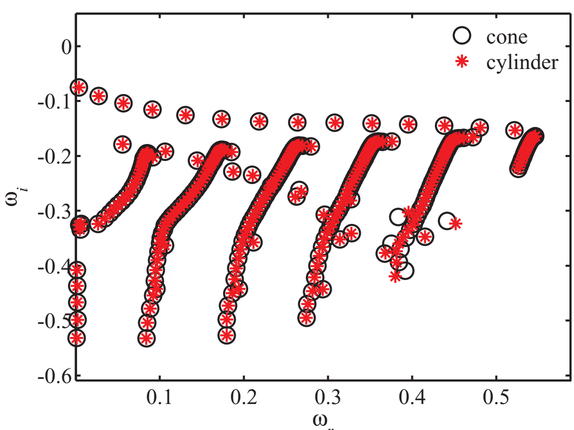

FIG. 8. Eigenspectrum comparison of the global stability analysis for the incompressible boundary layer flow over the circular cylinder and cone with extrapolation conditions at the outflow boundary. The Reynolds number is Re $= 1000$ based on the body radius.

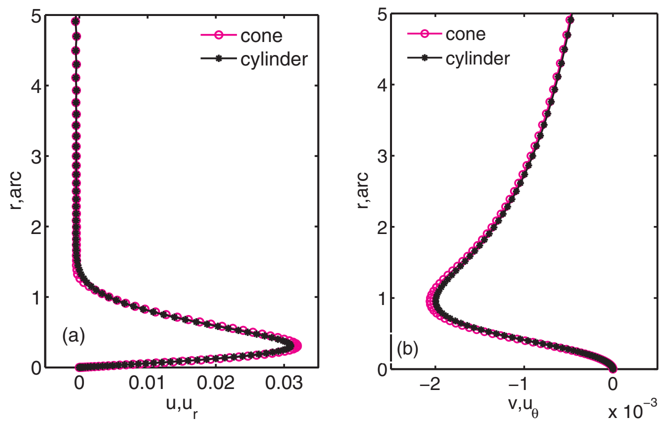

FIG. 9. Eigenfunction comparison of the global stability analysis for the incompressible boundary layer flow over the circular cone and cylinder with extrapolation boundary conditions at the outflow for Re = 1000 at streamwise distance $x = r = 90$ for (a) streamwise disturbances u and (b) wall-normal disturbances v. Here u and v are the streamwise and wall-normal disturbances for both cylindrical and spherical coordinates.

parts of the eigenvalues show a monotonic convergence of the solution with the increased resolution. In Table II n and m indicate the number of collocation points in the radial and polar directions, respectively. The relative error ϵ is computed between two consecutive grid sizes for real and imaginary parts. The largest associated error between both eigenmodes is considered. Mesh 1 is used in all the results of stability computations reported here.

B. Evaluation of the boundary conditions

Global stability analysis was performed for the axisymmetric ($N = 0$) mode and Re = 349 with two different outflow boundary conditions: linear extrapolation and Neumann boundary conditions. The Dirichlet boundary conditions are considered for velocity disturbances at the inflow boundary. The streamwise domain length is taken as $L_r = 214.9$. Figure 10 shows a comparison of the discrete part of the spectrum for two different boundary conditions. It shows that the temporal growth rate ω_i is the same for the least stable eigenmode; however, the variation in the ω_i value increases with an increase in frequency ω_r for both boundary conditions. The least stable eigenmode near the frequency $\omega_r = 0.005$ as marked by the rectangle in Fig. 10 is selected and spatial eigenmodes u_r and u_θ are plotted at the same streamwise location $r = 92$ for both boundary conditions as shown in Fig. 11. It shows that the spatial eigenmodes are almost the same for both exit boundary conditions. Thus, the qualitative features of the global stability results are not affected here by the choice of

TABLE II. Grid convergence study for two leading eigenvalues ω_1 and ω_2 for $R_e = 349$, azimuthal wave number $N = 1$, and semicone angle $\alpha = 2^\circ$ for different grid sizes. The grid refinement ratio in each direction is 1.14. The maximum relative error is shown here. The dimensions of the computational domain in spherical coordinates are $L_r = 214.9$ and $L_\theta = 12^\circ$ for global stability computations.

Mesh	$n \times m$	ω_1	ω_2	error (%)
1	121×121	$0.01528 - 0.03609i$	$0.02869 - 0.04375i$	0.174
2	107×107	$0.01528 - 0.03610i$	$0.02874 - 0.04374i$	0.243
3	93×93	$0.01530 - 0.03616i$	$0.02881 - 0.04379i$	

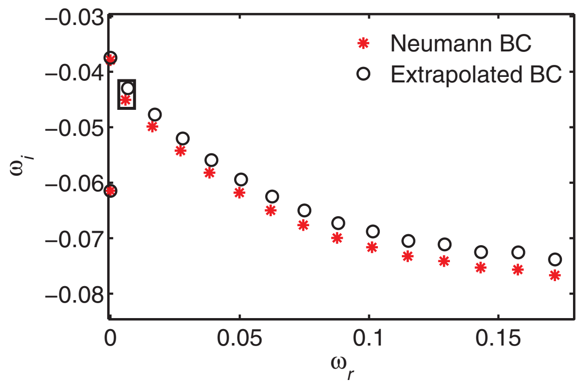

FIG. 10. Comparison of the eigenspectrum resulting from the global stability analysis of the boundary layer over a circular cone for semicone angle $\alpha = 2^{\circ}$, $N = 0$, and Re $= 349$ for different outlet boundary conditions (BCs).

boundary conditions. Hence, the extrapolation type of condition is chosen at the outflow boundary in all global stability computations because it is less restrictive in nature, as suggested by Theofilis [2].

C. Influence of domain length L_r

To check the effect of domain length L_r on the global stability results, the global stability computations are performed with the two different domain lengths $L_r = 214.9$ and 243.6 for semicone angle $\alpha = 2^{\circ}$, axisymmetric mode ($N = 0$), and Re $= 349$. The Dirichlet and extrapolation boundary conditions are considered at the inflow and outflow boundaries, respectively. Figure 12 represents the discrete spectrum (TS modes) resulting from the global stability analysis for two different domain lengths. The discretization of the frequency comes from the truncation of the domain and hence the domain length always affects the resulting spectrum [25]. Figure 12 shows that the space between the frequency decreases with an increase in domain length and may approach zero with an infinite domain length. In order to check the effect of the domain length on the global stability results, the two leading eigenmodes are selected as marked by the squares in Fig. 12 with

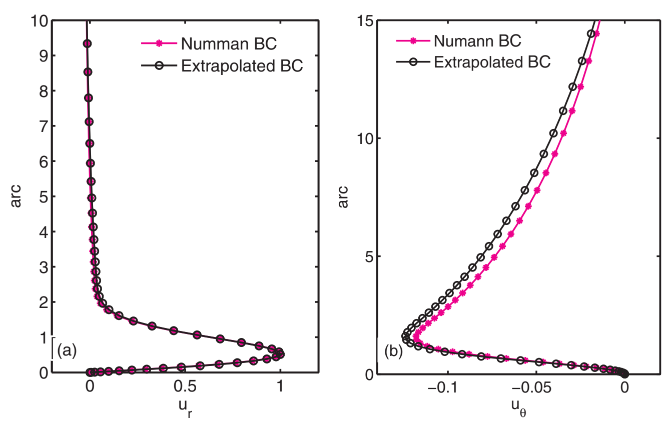

FIG. 11. Eigenfunction comparison for the global stability analysis of the incompressible boundary layer over a circular cone for $\alpha = 2^{\circ}$, $N = 0$, and Re $= 349$ at the streamwise location $r = 92$ for (a) u_r and (b) u_θ as marked by the rectangle in Fig. 10.

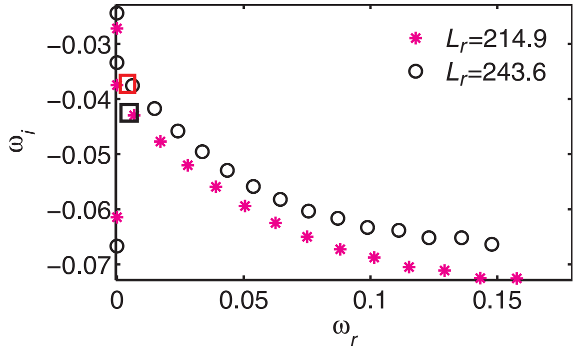

FIG. 12. Comparison of the eigenspectrum resulting from the global stability analysis of the boundary layer over a circular cone for semicone angle $\alpha = 2^\circ$, $N = 0$, and Re $= 349$ for different domain lengths.

frequency near $\omega_r = 0.006$. Figure 13 shows a comparison of the eigenfunctions u_r and u_θ for two different domain lengths. The eigenfunctions are in good agreement, which shows that the domain length $L_r = 214.9$ is sufficient to apply the extrapolation condition at the outflow boundary. Thus, the global stability results presented here are independent of the domain length as well as the outflow boundary conditions.

D. Semicone angle $\alpha = 2^\circ$

Figure 14 shows the eigenspectrum of the axisymmetric mode ($N = 0$) for Re $= 349$ and semicone angle $\alpha = 2^\circ$. The eigenmodes marked by the square and the circle are called stationary and oscillatory modes, respectively. This stationary mode has a complex frequency $\omega = 0 - 0.02667i$. The global mode is temporally stable because $\omega_i < 0$ and hence the amplitudes of the disturbances decay in time. Figures 15(a) and 15(b) presents the two-dimensional spatial structure of the eigenmodes for radial (u_r) and polar (u_θ) velocity disturbances. The magnitudes of the disturbance amplitudes are zero at the inlet as it is applied to the inlet boundary condition. The disturbance amplitudes evolve with time in the flow domain and move in the streamwise direction downstream. The size and magnitudes of the disturbances grow as they move downstream. The magnitudes of the u_r disturbances are one order higher than those of u_θ. The polar disturbance u_θ contaminates

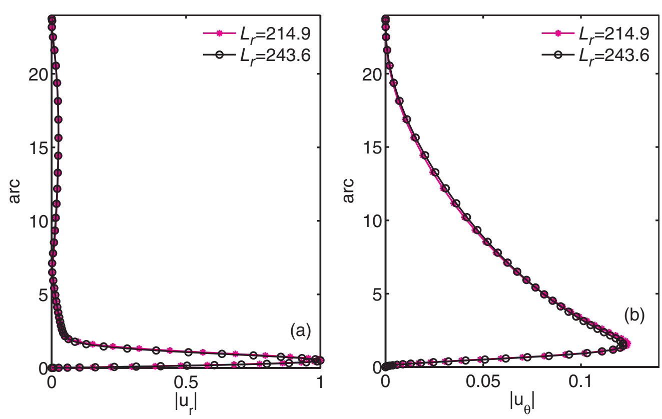

FIG. 13. Eigenfunction comparison for the global stability analysis of the incompressible boundary layer flow over a circular cone for $\alpha = 2^\circ$, $N = 0$, and Re $= 349$ at the streamwise location $r = 141$ for (a) u_r and (b) u_θ as marked by the square in Fig. 12.

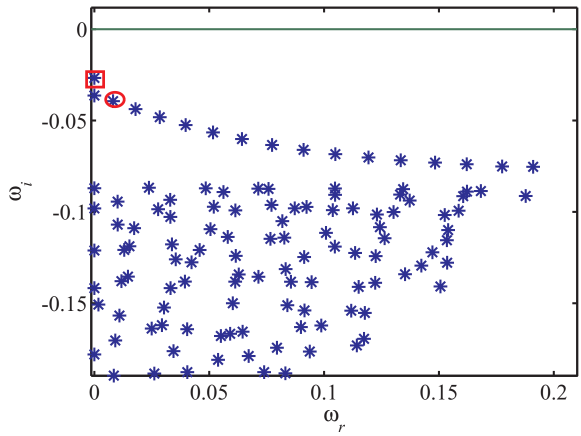

FIG. 14. Eigenspectrum for the axisymmetric mode ($N = 0$) and Re $= 349$ for semicone angle $\alpha = 2^{\circ}$.

the flow field to a greater extent than that the u_r disturbance; however, the magnitude is very small compare to u_r. Figure 16 shows the spatial structure of the oscillatory eigenmode. The associated complex frequency for this mode is $\omega = 0.008154 - 0.03937i$. This oscillatory global mode is also temporally stable, because $\omega_i < 0$. The variation of the amplitude is not monotonic for this eigenmode. The wavelike nature of the disturbances is found for this mode. The oscillatory modes evolving in the flow field grow in size and magnitude while moving downstream and hence the flow is convectively unstable. Figure 17 shows the two-dimensional mode structure of u_r and u_θ for $\omega_r = 0.1775$. The streamwise domain length is $L_r = 214.9$. The disturbances are observed to evolve near the wall surface and decay exponentially at the freestream. The typical length scale of the wavelet structure decreases with an increase in frequency ω_r. It also demonstrates that the region of contamination is reduced with an increase in frequency. The length scale of the wavelet structure is found to be small for the increased frequency, as shown in Fig. 17.

E. Semicone angle $\alpha = 4^{\circ}$

Figure 18 shows the spectrum for the helical mode $N = 1$, Re $= 523$, and semicone angle $\alpha = 4^{\circ}$. The most unstable oscillatory mode has an eigenvalue $\omega = 0.01942 - 0.05512i$. The global mode is temporally stable because the largest $\omega_i < 0$. Figure 19 shows the two-dimensional mode structure

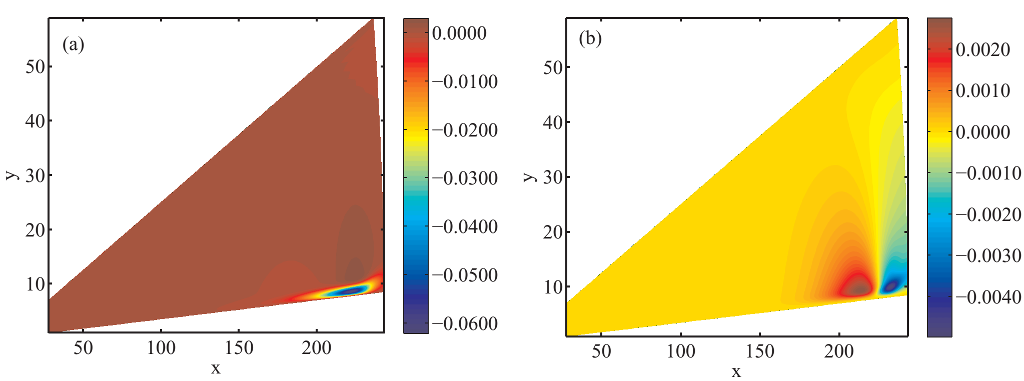

FIG. 15. Contour plot of the real parts of (a) streamwise u_r and (b) wall-normal u_θ velocity disturbances for the stationary eigenmode, with $\omega = 0 - 0.02667i$ for semicone angle $\alpha = 2^{\circ}$ marked by the square in Fig. 14.

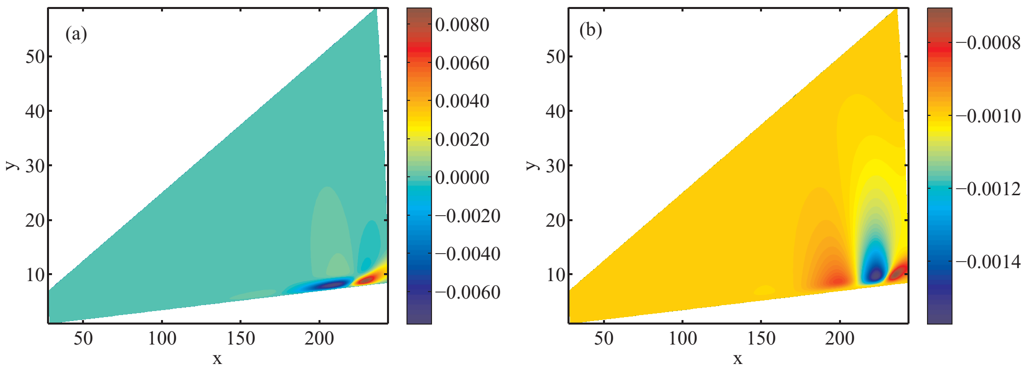

FIG. 16. Contour plot of the real parts of (a) streamwise u_r and (b) wall-normal u_θ velocity disturbances for the oscillatory eigenmode, with $\omega = 0.008154 - 0.03937i$ for semicone angle $\alpha = 2^\circ$ as marked by the ellipse in Fig. 14.

for $N = 1$, Re $= 523$, and semicone angle $\alpha = 4^\circ$. It has been observed that the disturbances evolved in the flow field at an earlier stage than that of a cone with semicone angle $\alpha = 2^\circ$. The magnitudes of the disturbance velocity components and the region of contamination in the polar direction are higher than those of $\alpha = 2^\circ$, which makes the flow convectively more unstable. The largest ω_i has been reduced with the increased semicone angle α for a given Reynolds number, which makes the global modes more stable.

F. Semicone angle $\alpha = 6^\circ$

Figure 20 shows the spectrum for the helical mode $N = 1$, Re $= 698$, and semicone angle $\alpha = 6^\circ$. The most unstable oscillatory mode has an eigenvalue $\omega = 0.02539 - 0.07707i$. The global mode is temporally stable because the largest $\omega_i < 0$. Figure 21 shows the two-dimensional mode structure for $N = 1$, Re $= 698$, and semicone angle $\alpha = 6^\circ$. The structure of the discrete part of the spectrum is disturbed with an increase in semicone angle α. The magnitudes of the u_r disturbance amplitudes is one order higher than those of u_θ and u_Φ. With an increase in semicone angle α the disturbances start to grow at an early stage. It has been observed that the disturbances evolved in the flow field

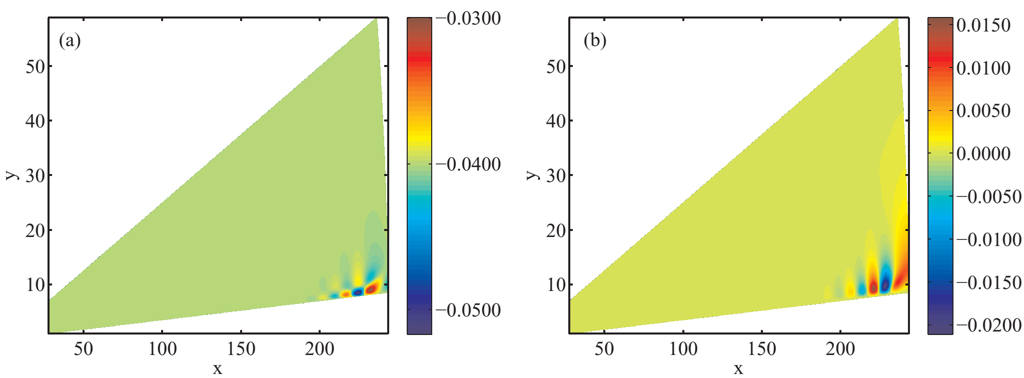

FIG. 17. Contour plot of the real parts of (a) streamwise u_r and (b) wall-normal u_θ velocity disturbances for the oscillatory eigenmode, with $\omega = 0.1775 - 0.07512i$ for semicone angle $\alpha = 2^\circ$.

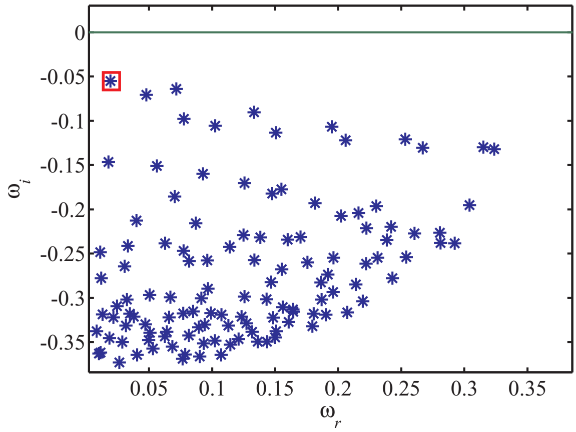

FIG. 18. Eigenspectrum for the helical mode ($N = 1$) and Re $= 523$ for semicone angle $\alpha = 4^{\circ}$.

at an earlier stage than those of a cone with semicone angle $\alpha = 2^{\circ}$. The spatial structures of the disturbances are of similar nature; however, the damping rate of the global mode increases with an increase in semicone angle.

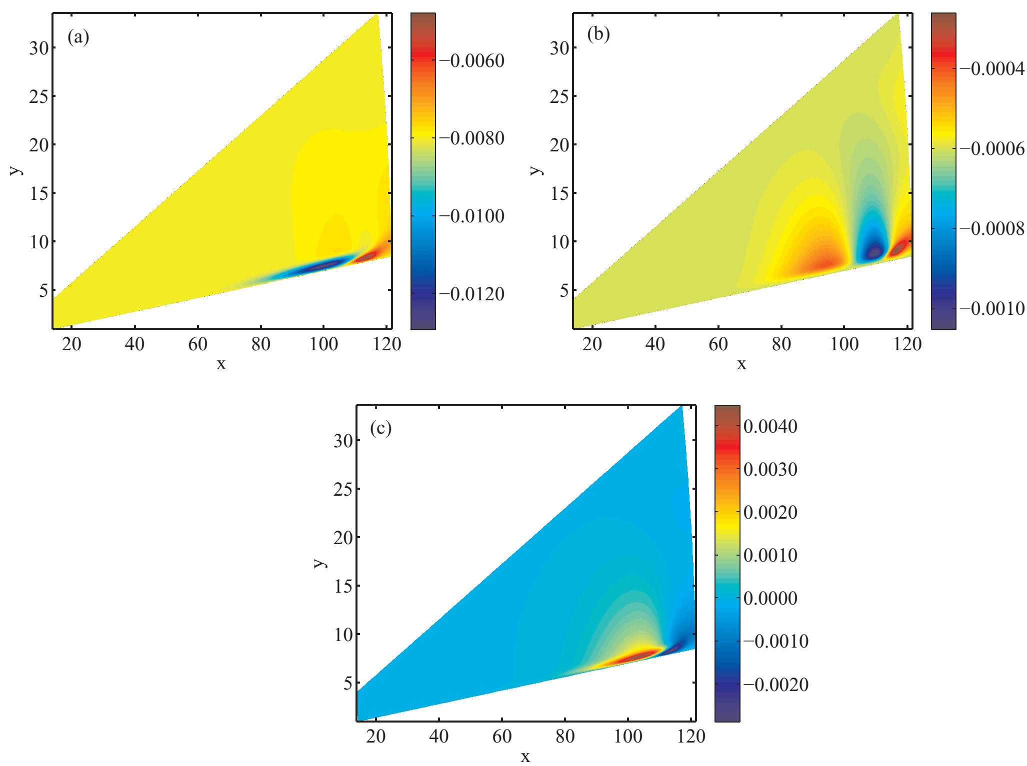

FIG. 19. Contour plot of the real parts of (a) streamwise u_r, (b) wall-normal u_θ, and (c) azimuthal u_ϕ velocity disturbances for the stationary eigenmode, with $\omega = 0.01942 - 0.05512i$ for semicone angle $\alpha = 4^{\circ}$ marked by the square in Fig. 18.

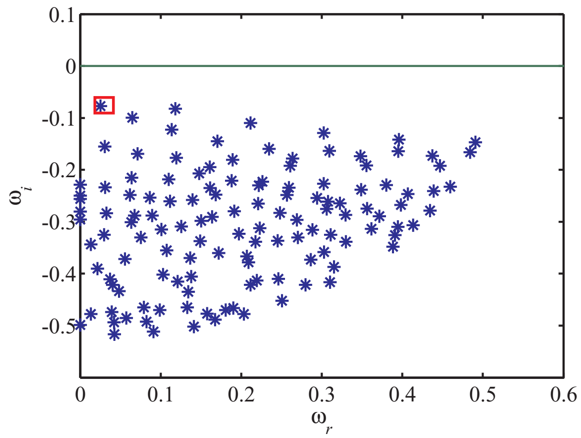

FIG. 20. Eigenspectrum for the helical mode ($N = 1$) and Re $= 698$ for semicone angle $\alpha = 6^\circ$.

G. Temporal growth rate

Figure 22 shows the temporal growth rate of the least stable eigenmodes for different Reynolds number and semicone angles α. The growth rate of eigenmodes increases with the increase in Reynolds number for all azimuthal wave numbers N and semicone angles. For the range of Reynolds

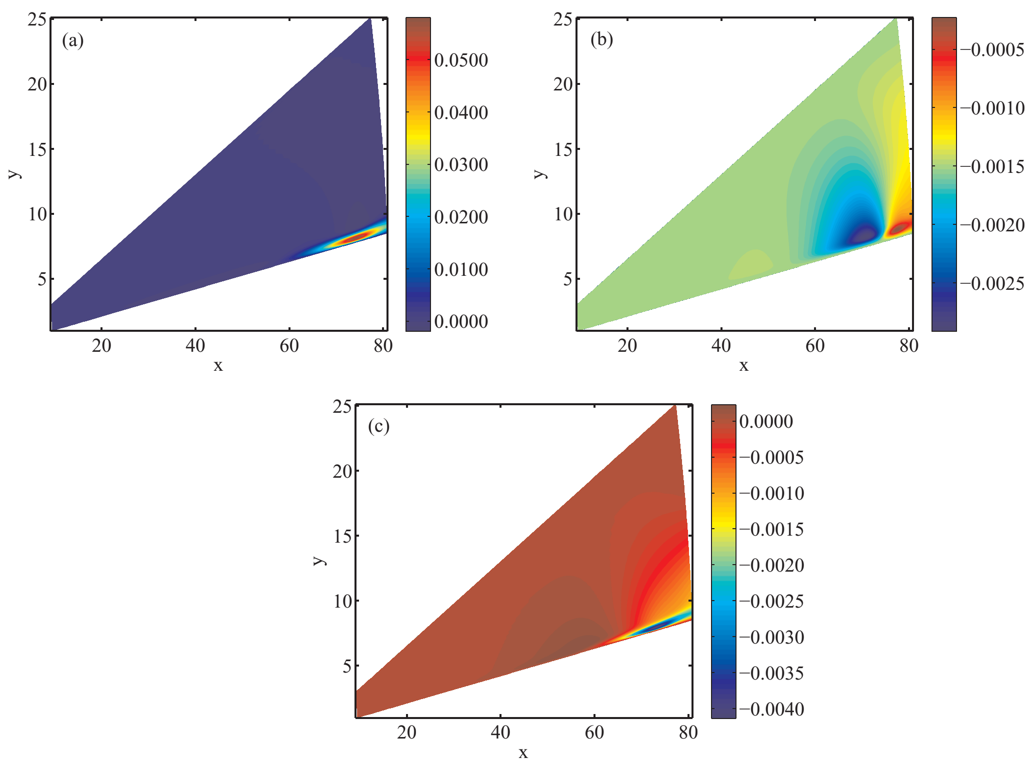

FIG. 21. Contour plot of the real parts of (a) streamwise u_r, (b) wall-normal u_θ, and (c) azimuthal u_ϕ velocity disturbances for the stationary eigenmode, with $\omega = 0.02539 - 0.07707i$ for semicone angle $\alpha = 6^\circ$ marked by the square in Fig. 20.

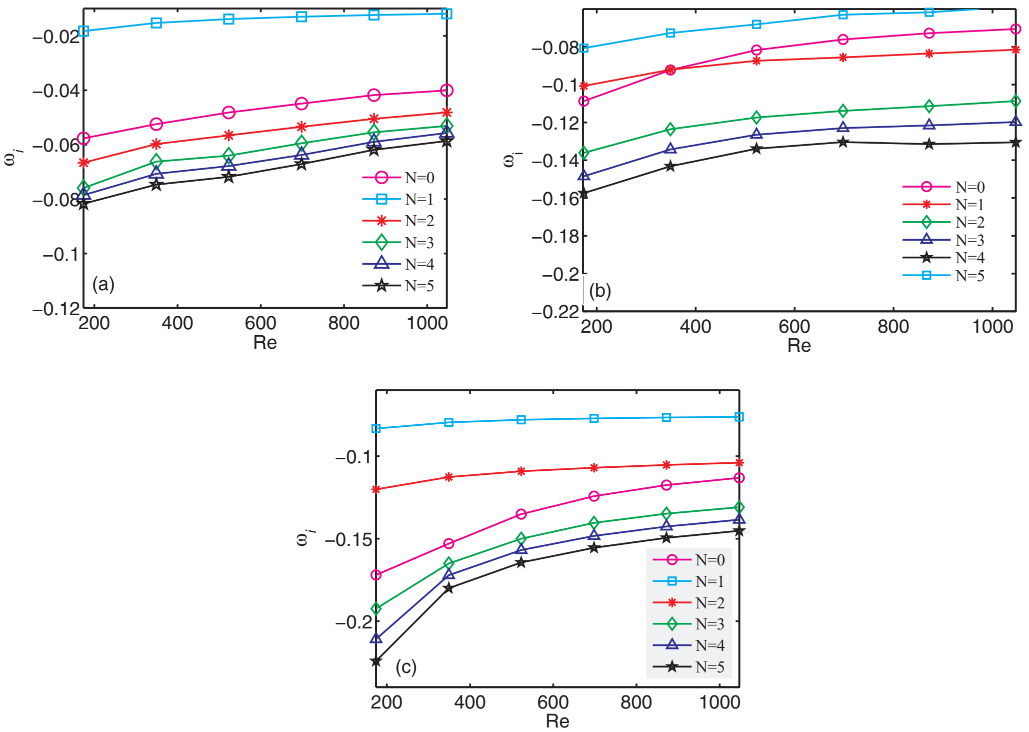

FIG. 22. Variation in temporal growth rate ω_i with the Reynolds number for different semicone angles (a) $\alpha = 2°$, (b) $\alpha = 4°$, and (c) $\alpha = 6°$.

number and semicone angles the least stable eigenmodes are negative, hence the global modes are stable. The global modes with helical mode $N = 1$ are least stable for $\alpha = 2°$, $4°$, and $6°$. The damping rate of global modes with $N = 2$ is higher than with $N = 0$ for $\alpha = 2°$. At smaller Re, $N = 0$ is more stable than $N = 2$; however, at higher Re, $N = 2$ is more stable than $N = 0$ for semicone angle $\alpha = 4°$. The helical modes $N = 3$, 4, and 5 have larger damping rates than those of $N = 0$, 1, and 2 for all Re and α. The global modes are more stable at higher semicone angle α. The transverse curvature reduces in the streamwise direction with an increase in Reynolds number for the same α. The favorable pressure gradient is higher at higher semicone angle α. The global modes are more stable at higher semicone angle, proving that a favorable pressure gradient has a damping effect on the global modes.

H. Spatial amplification rate

Global temporal modes exhibit growth or decay in the streamwise direction while moving downstream. This growth or decay at a different streamwise station can be quantified by the spatial amplification rate A_x. The spatial amplification rate A_x shows the growth of all the disturbances together in the streamwise direction. Figure 23 shows the A_x for different azimuthal wave numbers N and semicone angles α for Re = 349. The spatial growth rate A_x increases with an increase in semicone angle α for all the azimuthal wave numbers for a given Reynolds number. We computed it for Re = 174–1047; however, the result are presented for Re = 349 only. As the semicone angle α increases, the growth rate of the disturbances increases in the streamwise direction and makes the flow convectively unstable. Hence, at higher semicone angle flow becomes convectively more unstable. For $N = 0$, 1, and 2 the disturbances exhibit higher spatial growth rate at small

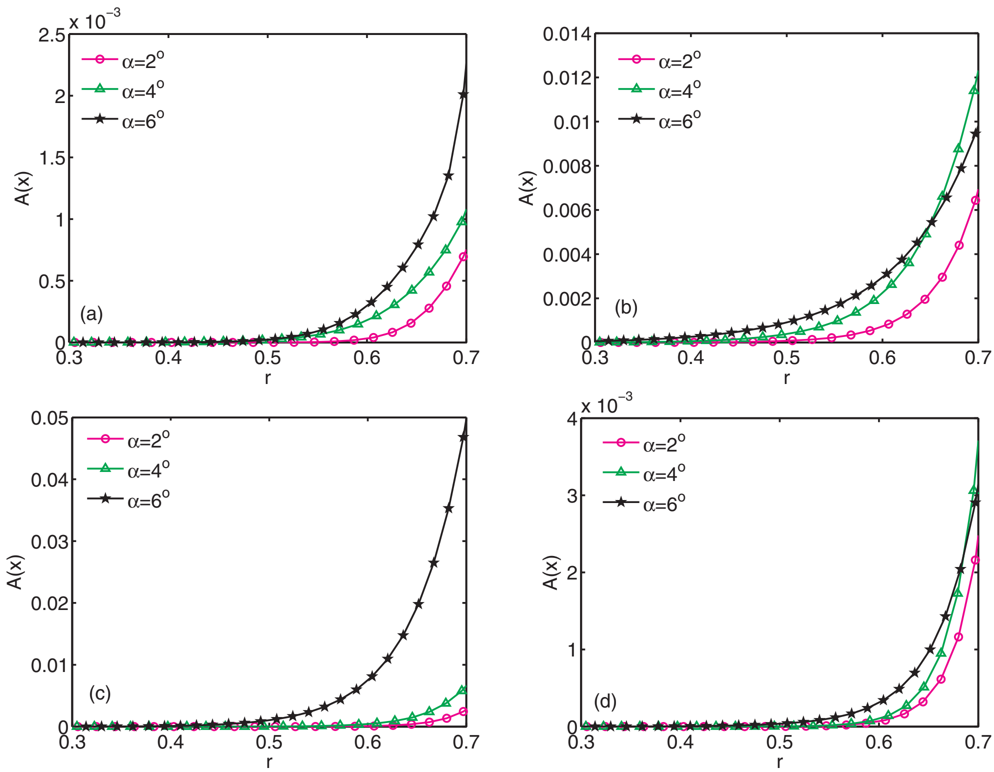

FIG. 23. Variation of spatial growth rate A_x in the streamwise direction for different semicone angles α for Re $= 349$: (a) $N = 0$, (b) $N = 1$, (c) $N = 2$, and (d) $N = 3$.

Reynolds number; however, for $N = 3$, 4, and 5 the spatial growth rate is high for higher Reynolds number.

VI. CONCLUSIONS

Linear global stability analysis of the boundary layer formed on a circular cone was performed. The combined effect of transverse curvature and pressure gradient has been studied. The global temporal modes were computed for the axisymmetric boundary layer on a circular cone for a range of Reynolds number from 174 to 1046 with azimuthal wave number N from 0 to 5 and semicone angles $\alpha = 2^\circ$, 4°, and 6°. The largest imaginary part ω_i of the computed global modes is negative for all Reynolds numbers Re, azimuthal wave numbers N, and semicone angles α. Hence, the global modes are temporally stable. The wavelike behavior of the eigenmodes is found in the streamwise direction. The wavelength of the wavelet structure decreases with an increase in frequency ω_r. The 2D spatial structure of the global modes shows that the size and magnitude of the disturbance amplitudes increase while downstream, which proves that the flow is convectively unstable. The damping rate of the disturbances increases with an increase in semicone angle α from 2° to 6°. Thus, global modes are more stable at higher α. At the same time, with an increase in α from 2° to 6°, the spatial growth rate A_x also increases at a given Reynolds number, thus the flow becomes convectively more unstable at higher semicone angles. The azimuthal wave numbers $N = 3$, 4, and 5 have less temporal growth ω_i and spatial growth A_x compared to $N = 0$, 1, and 2. The azimuthal wave number $N = 1$ is found to be the least stable one for all Re and α. The increase in α develops a favorable pressure gradient and reduces the transverse curvature effect. Thus, the favorable pressure gradient stabilizes the global modes and the effect of transverse curvature decreases. Thus, the role of a favorable pressure gradient is more effective than that of transverse curvature on flow stability.

ACKNOWLEDGMENT

We would like to thank Aeronautics Research and Development Board, Government of India, for financial support for this project.

---

[1] P. Drazin and W. Raid, *Hydrodynamic Stability* (Cambridge University Press, Cambridge, 2004).
[2] V. Theofilis, Advances in global linear instability analysis of nonparallel and three dimensional flows, Prog. Aerosp. Sci. **39**, 249 (2003).
[3] G. N. V. Rao, Mechanics of transition in an axisymmetric laminar boundary layer on a circular cylinder, J. Appl. Math. Phys. **25**, 63 (1974).
[4] O. Tutty and W. Price, Boundary layer flow on a long thin cylinder, Phys. Fluids **14**, 628 (2002).
[5] N. Vinod, Stability and transition in boundary layers: Effect of transverse curvature and pressure gradient, Ph.D. thesis, Jawaharlal Nehru Centre for Advanced Scientific Research, 2005.
[6] M. R. Malik and D. I. A. Poll, Effect of curvature on three dimensional boundary layer stability, AIAA J. **23**, 1362 (1985).
[7] N. Vinod and R. Govindarajan, Secondary instabilities in incompressible axisymmetric boundary layers: Effect of transverse curvature, J. Fluid Eng. **134**, 024503 (2012).
[8] G. Petrov, Boundary layer on a rotating cylinder in axial flow, J. Appl. Mech. Tech. Phys. **17**, 506 (1976).
[9] K.-H. Kao and C.-Y. Chao, Stability of a boundary layer on a spinning semi-infinite circular cylinder, J. Spacecraft Rockets **28**, 284 (1991).
[10] M. A. Herrada, C. Del Pino, and R. Fernandez-Feria, Stability of the boundary layer flow on a long thin rotating cylinder, Phys. Fluids **20**, 034105 (2008).
[11] S. D. Muralidhar, B. Pier, J. F. Scott, and R. Govindarajan, Flow around a rotating, semi-infinite cylinder in an axial stream, Proc. R. Soc. A **472**, 20150850 (2016).
[12] L. M. Mack, *Proceedings of the 19th AIAA, Fluid Dynamics, Plasma Dynamics, and Lasers Conference* (AIAA, Reston, 1987), paper 1987-1413.
[13] M. Malik, Numerical methods for hypersonic boundary layer stability, J. Comput. Phys. **86**, 376 (1990).
[14] M. R. Malik and R. E. Spall, On the stability of compressible flow past axisymmetric bodies, J. Fluid Mech. **228**, 443 (1991).
[15] P. W. Duck, The effect of the surface discontinuity on a axisymmetric boundary layer, Quart. J. Mech. Appl. Math. **37**, 57 (1984).
[16] P. W. Duck and P. Hall, On the interaction of Tollmein-Schlichting waves in axisymmetric supersonic flows, Quart. J. Mech. Appl. Math. **42**, 115 (1989).
[17] P. W. Duck, The inviscid axisymmetric stability of the supersonic flow along a circular cylinder, J. Fluid Mech. **214**, 611 (1990).
[18] P. W. Duck and S. J. Shaw, The inviscid stability of supersonic flow past a sharp cone, Theort. Comput. Fluid Dynamics. **2**, **139** (1990).
[19] L. M. Mack, Boundary layer linear stability theory, AGARD Report No. 709, 1984 (unpublished).
[20] K. F. Stetson and R. L. Kimmel, *Proceedings of the 30th AIAA Aerospace Sciences Meeting & Exhibit* (AIAA, Reston, 1992), paper 1992-0737.
[21] K. F. Stetson and R. Kimmel, *Proceedings of the 31st AIAA Aerospace Sciences Meeting & Exhibit* (AIAA, Reston, 1993), paper 1993-0896.
[22] A. Maslov, S. Mironov, A. Shiplyuk, V. Aniskin, D. Buntin, and A. Sidorenko, *Proceedings of the 40th AIAA Aerospace Sciences Meeting & Exhibit* (AIAA, Reston, 2002), paper 2002-0153.
[23] T. J. Horvath, S. A. Berry, B. R. Hollis, C. L. Chang, and B. A. Singer, *Proceedings of the 32nd AIAA Fluid Dynamics Conference & Exhibit* (AIAA, Reston, 2002), paper 2002-2743.

[24] E. Akervik, U. Ehrenstein, F. Gallaire, and D. S. Henningson, Global two-dimensional stability measure of the flat plate boundary-layer flow, Eur. J. Mech. B **27**, 501 (2008).

[25] F. Alizard and J. C. Robinet, Spatially convective global modes in a boundary layer, Phys. Fluids **19**, 114105 (2007).

[26] U. Ehrenstein and F. Gallaire, On two-dimensional temporal modes in spatially evolving open flows: The flat-plate boundary layer, J. Fluid Mech. **536**, 209 (2005).

[27] V. Theofilis, Global linear instability, Annu. Rev. Fluid Mech. **43**, 319 (2011).

[28] H. F. Fasel, U. Rist, and U. Konzelmann, Numerical investigation of the three -dimensional development in boundary layer transition, AIAA J. **28**, 29 (1990).

[29] G. Swaminathan, K. C. Sahu, A. Sameen, and R. Govidarajan, Global instabilities in diverging channel flows, Theor. Comput. Fluid Dyn. **25**, 53 (2011).

[30] R. Bhoraniya and N. Vinod, Global stability analysis of axisymmetric boundary layers over a circular cone, J. Phys.: Conf. Ser. **822**, 012018 (2017).

[31] B. Costa, W.-S. Don, and A. Simas, in *Proceedings of SCPDE: Recent Progress in Scientific Computing*, edited by W. Liu, M. Ng, and Z.-C. Shi (Science, Beijing, 2007), pp. 179–188.

[32] P. J. Roache, A method for uniform reporting of grid refinement studies, J. Fluid Eng. **116**, 405 (1994).

[33] S. J. Garrett and N. Peake, The absolute instability of the boundary layer on rotating cone, Eur. J. Mech. B **26**, 344 (2007).

[34] R. Bhoraniya and N. Vinod, Global stability analysis of axisymmetric boundary layers, Theor. Comput. Fluid Dyn. (to be published) (2017).